Chapter 2

Terahertz Nanoantennas for Enhanced Spectroscopy

Riccardo Piccoli, Andrea Rovere, Andrea Toma,
Roberto Morandotti and Luca Razzari

Additional information is available at the end of the chapter

http://dx.doi.org/10.5772/66349

Abstract

Terahertz spectroscopy has great potential for sensing a wide range of elementary excitations. However, terahertz studies are practically limited to macroscopic ensembles of compounds (e.g., thick pellets of crystallized molecules or highly concentrated solutions of nanomaterials) due to the long radiation wavelength (about 300 μm at 1 THz). In this chapter, we show how terahertz nanoantennas can overcome the current limitations of terahertz spectroscopy such as low sensitivity and low spatial resolution. We briefly discuss how to design the resonance characteristics of a dipole nanoantenna through a Fabry-Pérot model, and then we present the experimental characterization of the spectral response of ordered arrays of such devices. Furthermore, we demonstrate how nanoantenna arrays enable the possibility of retrieving the spectroscopic signature of a monolayer of quantum dots and, in principle, of many other organic or inorganic compounds. This technique, based on the idea of increasing the sensitivity through local field enhancement, is named *nanoantenna-enhanced terahertz spectroscopy* (NETS). A Fano-like interference between the fundamental mode of the nanoantennas and the phonon resonance of the quantum dots is observed, together with an enhancement of the absorption of the dots up to more than a million. Finally, we show how to extract the main spectroscopic information of the quantum dots through a simple coupled harmonic oscillator model. This novel technique can be widely applied in terahertz spectroscopic studies of nanocrystals and molecules, where extremely low concentrations are of concern.

Keywords: surface enhancement, terahertz spectroscopy, nanoantennas

1. Introduction

Terahertz (THz) spectroscopy is a promising technique for sensing low-frequency modes (e.g., collective vibrations, phonons, magnons, intra-excitonic transitions) of a variety of materials and compounds [1]. However, some of the main drawbacks of THz spectroscopy are its extremely low sensitivity and the difficulty to sense nano-objects as well as ultra-low amount of chemical compounds, due to the long radiation wavelength and the associated diffraction limitations. Recently, several research groups devoted their efforts to investigate metamaterials [2–4] and nanoslot-based [5–7] platforms tailored for the THz sensing of, for example, small molecules such as lactose, fructose, sucrose [6, 7] or microorganism such as fungi and bacteria [2]. However, THz studies employing these techniques were not able to provide any spectral information regarding the investigated specimen. In the last decades, *surface enhancement* [8] methods were widely explored, given the associated capability of increasing the sensitivity of traditional spectroscopies. More in detail, *surface-enhanced Raman spectroscopy* (SERS) was first developed [9, 10] and has been proven to be an effective tool for investigations down to the single molecule level [11–13]. Afterward, *surface-enhanced infrared absorption* (SEIRA) [14, 15] was proposed for direct absorption spectroscopy in the infrared region, enabling the study of molecules at the sub-attomolar level [16]. The central idea of these techniques stems from the fact that both Raman and absorption spectroscopies are sensitive to the local electric field, which can be significantly amplified on rough metal surfaces or in proximity of metallic nanostructures [17]. In this chapter, we show how the use of properly engineered metallic nanostructures can overcome the current limitations of THz spectroscopy, such as low spatial resolution and sensitivity. Indeed, the distinctive ability of metallic nanoantennas [18] to collect and concentrate incident light beyond the diffraction limit allows achieving high local fields, thus intensifying radiation-matter interactions by order of magnitudes. In Section 2.1, we provide the basic concepts for the design of the resonant properties of nanoantennas for THz light. In particular, we introduce the Drude model for the description of the complex dielectric function [19] of a conductor, and then, we present a simple quasi-analytical model to describe the antenna behavior as a Fabry-Pérot resonator [20]. Subsequently, in Section 2.2, we extend our investigation to the resonance properties of ordered arrays of THz dipole nanoantennas, both numerically and experimentally [21, 22]. In Section 3, after summarizing the recent discoveries and techniques regarding enhanced THz sensing, we demonstrate how arrays of dipolar nanoantennas can effectively be employed for THz spectroscopy, discussing what we have named: *nanoantenna-enhanced THz spectroscopy* (NETS) [23]. In particular, we present our test of NETS on a monolayer of cadmium selenide quantum dots, and by employing a simple model based on a mechanical analog (coupled harmonic oscillators), we show how to retrieve the main spectroscopic properties of the specimen under investigation. This technique enables unprecedented spatial localization of THz light and high sensitivity, which results in a new powerful tool for THz investigations of ultra-low amounts of compounds, potentially down to the single nano-object level.

http://dx.doi.org/10.5772/66349

2. Modeling, design and characterization of nanoantennas for terahertz light

2.1. Properties of metals and nanoantenna modeling at terahertz frequencies

In order to properly design and model THz nanoantennas, we first need to be able to describe the electromagnetic properties of a metal when it no longer behaves as a perfect conductor. In fact, already in the GHz domain, losses become an important constraint that microwave engineers have to deal with [18, 19]. In a first approximation, it is possible to retrieve the optical properties of a conductor by means of a simple model developed by Paul Drude in 1900, which considers the conducting material as an ideal gas of free electrons that move in a background of fixed positive ions. According to this picture, the valence electrons of the constituent atoms become conduction electrons and are able to freely move in the volume of the material. The complex dielectric function of the metal can therefore be obtained through a straightforward model describing the interaction of the electric field of the incoming radiation and this "sea" of electrons, which leads to the following expression [19]:

$$\varepsilon(\omega) = \varepsilon_1(\omega) + i\varepsilon_2(\omega) = \varepsilon_\infty - \frac{\omega_p^2}{\omega^2 + \gamma^2} + i\frac{\omega_p^2 \gamma}{\left(\omega^2 + \gamma^2\right)\omega} \quad \omega_p{}^2 = \frac{e^2 N}{m\varepsilon_0} \tag{1}$$

where ε_∞ is the dielectric constant at high frequencies, ω_p is the plasma frequency (N is the carrier concentration, e the electron charge, m the electron mass and ε_0 the vacuum permittivity) and $\gamma = 1/\tau$ is the Drude scattering rate (τ is the carrier lifetime). As one can see, in this model, the complex dielectric function and consequently all the others optical parameters (i.e., the refractive index and the conductivity) are fully characterized by the material plasma frequency and scattering rate [19]. Since the plasma frequency of noble metals lies in the visible UV region (e.g., for gold, $\omega_p/2\pi = 2067$ THz ; for silver, $\omega_p/2\pi = 2321$ THz [24]), at THz frequencies ($\omega \ll \omega_p$), the real part of the permittivity ε_1 results to be negative and significantly large in modulus. It is worth reminding that a finite and negative ε_1 is a fundamental requirement for the existence of a surface wave (named *surface plasmon polariton* [19] at optical frequencies) at the interface between a conductor and an insulator. The classical Drude model can be extended in order to consider the quantum nature of the carriers by introducing the *Drude-Sommerfeld model* [19]. The main consequence of this model in the derivation of the permittivity of metals is that, under an applied electric field, the carriers move in the material with an effective mass m_{eff}, which simply substitutes the free electron mass in the plasma frequency and conceptually incorporates the interaction between the lattice of positive ions and the sea of electrons. Finally, it is possible to take into account the contributions of bound electrons to the permittivity by using the *Drude-Lorentz model* [19], which assumes the presence of a restoring force between the carriers and the ions. In the most general scenario, considering a number k of real electronic transitions, we can therefore add to the complex dielectric function

in Eq. (1) a collection of damped harmonic oscillators with resonance frequencies $\omega_{0,k}$ as follows: $\omega_p^2 \sum_k f_k / (\omega_{0,k}{}^2 - \omega^2 - i\omega\gamma_{0,k})$, where $f_{k'}$ $\omega_{0,k}$ and $\gamma_{0,k}$ are the strength, the central frequency and the damping rate of the *kth* oscillator, respectively.

Taking advantage of the Drude description of the electromagnetic response of a metal and its extensions, we can develop a model able to predict the resonance characteristics of the basic element (i.e., a metallic nanoantenna) of the proposed NETS technique. This simplified model also allows a better understanding of the physical mechanism that gives rise to the optical response of such nanodevices. Let us consider the simplest nanoantenna geometry, a cylindrical wire of fixed radius *R* and length *L* (note that the cylindrical geometry is used to simplify the calculations, but the overall description is valid also for wires of arbitrary lateral section). Such wire can be described as a *Fabry-Pérot* resonator for a surface wave [18, 20], as illustrated in **Figure 1a**.

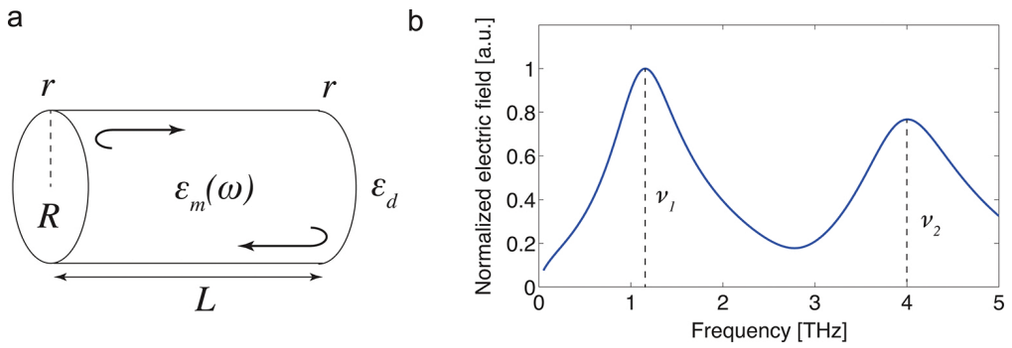

Figure 1. (a) Illustration for the modeling of a wire nanoantenna as a Fabry-Pérot resonator. (b) Normalized electric field amplitude at the tip of the nanoantenna obtained using Eq. (4) (permittivity of gold at THz frequencies taken from Ref. [32]).

For simplicity, we discuss only the propagation of the fundamental surface mode TM_0 (transverse magnetic, axially symmetric mode [18, 25]) along a thin metal wire with complex dielectric function $\varepsilon_m(\omega)$ (that can be extracted using the Drude description above). The wire is assumed to be surrounded by a dielectric medium of constant permittivity ε_d. The fundamental surface mode propagates along the antenna, and it is reflected at its ends, so that at specific frequencies standing waves (and the associated resonances) are formed, like in a traditional Fabry-Pérot resonator. These resonances occur when the antenna length is close to a multiple of half of the wavelength and, in particular, the lowest order resonance λ_{res} appears when the following relation is satisfied [26]:

$$\lambda_{res} / 2n_{eff} = L + 2\delta \tag{2}$$

where n_{eff} is the effective index of the propagating surface mode and δ is introduced to take into account the apparent increase of the antenna length, due to the reactance of the antenna

ends. The complex effective refractive index n_{eff} for a cylindrical wire can be derived from the Maxwell's equations by applying the proper boundary conditions at the dielectric—metallic cylinder interface [25], which leads to the following equation [27]:

$$\frac{\varepsilon_m}{k_m}\frac{I_1(\gamma_m R)}{I_0(\gamma_m R)}+\frac{\varepsilon_d}{k_d}\frac{K_1(\gamma_d R)}{K_0(\gamma_d R)}=0 \tag{3}$$

where I_j and K_j $(j=0,\ 1)$ are the modified Bessel functions, $\gamma_{m,d}=k_0\sqrt{n_{eff}^2-\varepsilon_{m,d}}$, $k_0=\omega/c$, c is the speed of light in vacuum and $k_{m,d}=\sqrt{n_{eff}^2-\varepsilon_{m,d}}$. The complex reflection coefficient r (thus including amplitude and phase) at the ends of the antenna can also be calculated in a closed-form for a subwavelength system, as detailed in Refs. [27, 28]. Basically, the electric and magnetic fields outside the antenna are expanded in terms of the free-space modes that are rotationally invariant (in order to preserve the symmetry of the problem). Then, the transverse electric and magnetic fields are matched at the interface (end of the antenna) to retrieve the reflection coefficient. Finally, we can calculate the electric field E_{tip} at the extremities of the wire antenna following the typical procedure used for a Fabry-Pérot cavity and considering that, for normal incidence, only the odd modes of the wire can be excited:

$$E_{tip}=E_0\frac{(1-re^{i\varphi})(1-e^{i\varphi})}{1-r^2e^{2i\varphi}} \qquad \varphi=k_0n_{eff}L \tag{4}$$

where E_0 is the field that couples at the tips of the nanoantenna and φ is the phase accumulated along the wire by the propagating surface mode in half round-trip. **Figure 1b** shows the resonance characteristics of a 100-μm-long gold wire nanoantenna (80 nm diameter) in vacuum, as obtained using Eq. (4). In this example, one can clearly see the first two (odd) modes of the nanoantenna, corresponding to the conditions $\lambda_1\approx 2n_{eff}L\left(\nu_1=\frac{c}{\lambda_1}\right)$ and $\lambda_2\approx 2n_{eff}L/3\left(\nu_2=\frac{c}{\lambda_2}\right)$, respectively.

2.2. Design, fabrication and characterization of nanoantenna arrays

The Fabry-Pérot model presented above allows an initial and insightful investigation of the resonance properties of a single nanoantenna. However, the proposed NETS technique makes use of far-field measurements to retrieve the spectral properties of the specimen under investigation. In order to guarantee an easily detectable signal in the far field, arrays of nanoantennas are commonly used. Short- and long-range interactions between neighboring nanoantennas lead to changes in the resonance characteristics of an array when compared to

a single isolated element [18]. In such scenario, a fine-tuning of the array resonances can be conducted by means of electromagnetic simulations, which allow taking into account the overall electromagnetic response of the system.

Once the proper architecture has been designed, it can be fabricated by employing electron-beam lithographic techniques. More specifically, for the arrays investigated in Refs. [21, 22], we used the following procedure: a 120-nm thick poly(methylmethacrylate) (PMMA) layer was spin-coated on a 500-μm thick, high-resistivity (>10 kΩcm) (100)-oriented silicon substrate. High-resistivity silicon was selected as a substrate since it is transparent and has a constant refractive index in the THz range. Charging effects that may occur during electron exposure over an insulating substrate have been prevented by means of a 10-nm-thick Al layer that was thermally evaporated on the PMMA surface. A high-resolution Raith150-Two e-beam writer at 15 keV beam energy and 520 μC/cm^2 exposure dose was used to prepare the nanoantenna patterns. After the Al removal in a KOH solution, the exposed resist was developed in MIBK/isopropanol (IPA) (1:3) for 30 s. Then, a 5-nm-thick adhesion layer of titanium was prepared using electron beam evaporation, with a 0.3-Å/s deposition rate in a high vacuum chamber (base pressure 10^{-7} mbar). In situ thermal evaporation (0.3-Å/s deposition rate) of a 60 nm gold film was obtained using a high temperature source mounted inside the vacuum chamber. After the film deposition, the unexposed resist was removed with acetone and rinsed out in IPA. The residual PMMA resist and organic contaminants were removed by means of O_2 plasma ashing for an improved lift-off. The two-dimensional arrays, composed of aligned nanoantennas with a fixed spacing G = 20 μm in both directions on the plane (see **Figure 2**), were fabricated on a 5 × 5 mm^2 area. In order to investigate the tunability of the resonance of such nanoantenna arrays in the THz range, we prepared a series of samples with different nanoantenna lengths (L = 30, 35, 40, 50 and 60 μm, respectively), fixed height (60 nm) and width (D = 200 nm).

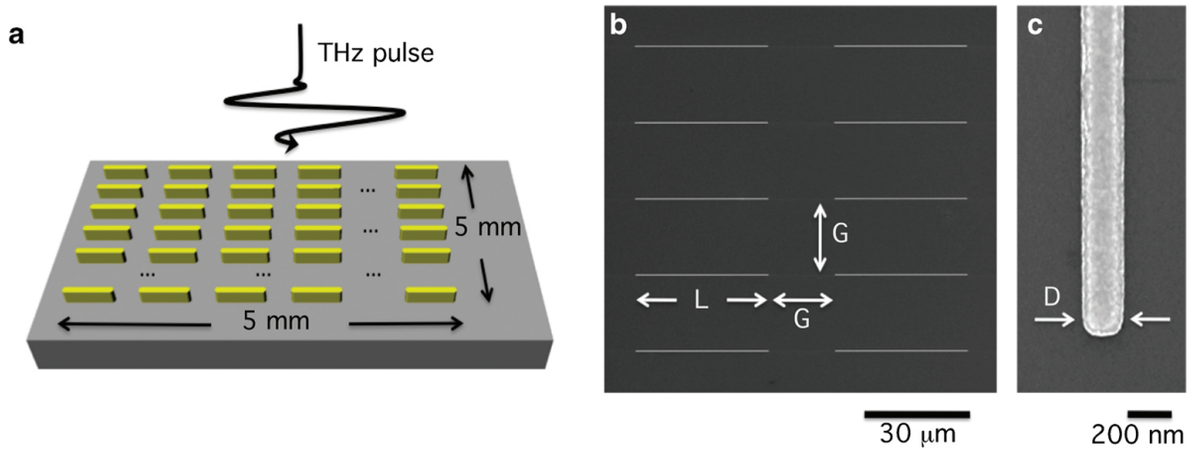

Figure 2. (a) Schematic illustration of the nanoantenna array. (b) SEM image of a detail of the array with L = 40 μm. (c) Magnification of the nanoantenna tip. Reproduced with permission from Ref. [22].

To characterize the spectral response of these samples, we employed a standard *time-domain spectroscopy* (TDS) setup [1]. In particular, THz pulses were generated via optical rectification of 130-fs-long pulses at 800 nm (1.6 mJ of energy at 1 kHz repetition rate) in a 500-μm-thick

http://dx.doi.org/10.5772/66349

(110)-ZnTe crystal. The arrays were placed in the collimated THz beam path (beam diameter of about 7 mm), and the transmitted radiation was then focused on a second ZnTe (500-μm thick) that was used to record the transmitted THz pulse trace in time, in a classical electro-optical sampling arrangement [29].

Because of the strong absorption of water molecules in the THz region, the measurements were performed in a nitrogen-purged environment. For the investigated arrays, the nanoantenna covering factor (defined as the ratio of the area covered by the nanoantennas to the total area of the array) is <1%, so that the transmitted spectrum when the THz radiation is polarized perpendicular to the nanoantenna main axis (nonresonant excitation) is found to be substantially equal to the one of a bare silicon substrate. For this reason, the array transmittance, named *relative transmittance* T_{rel}, can be simply calculated by dividing the spectrum collected exciting the nanoantennas with polarization aligned along their main axis (resonant excitation) by the one obtained under nonresonant excitation. The results of this procedure are shown in **Figure 3a**. As one can see, the transmission of the array is reduced up to 60% in correspondence of a resonance dip, which red-shifts by increasing the length L of the nanoantennas. From these data, we can estimate the nanoantenna *extinction efficiency* Q_{ext} as follows [21, 22]:

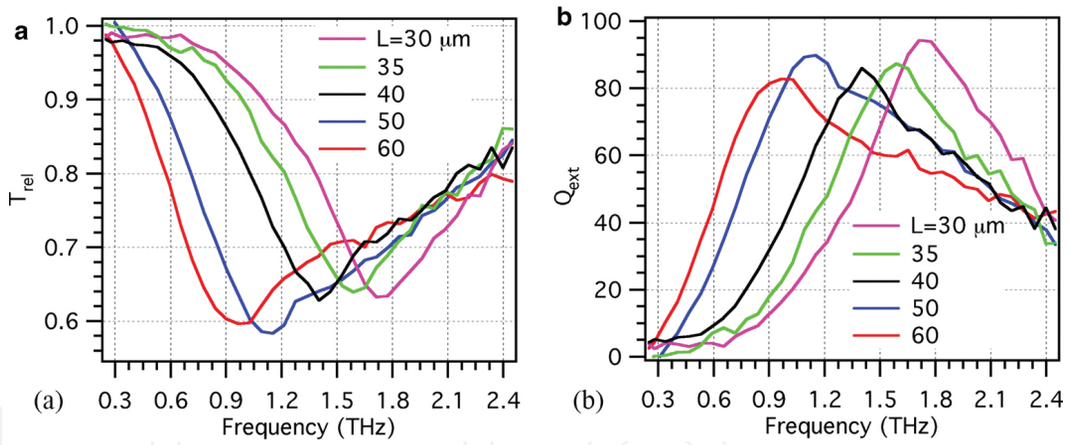

Figure 3. (a) Relative transmittance T_{rel} of the nanoantenna arrays as a function of frequency for the five samples with different nanoantenna lengths. (b) Extinction efficiency Q_{ext} as a function of frequency, calculated from the experimental data using Eq. (5). Reproduced with permission from Ref. [22].

$$Q_{ext} = \frac{\sigma_{ext}}{\sigma_{geo}} = \frac{A(1-T_{rel})}{NLD} = Q_{abs} + Q_{sca} = \frac{\sigma_{abs}}{\sigma_{geo}} + \frac{\sigma_{sca}}{\sigma_{geo}} \tag{5}$$

where σ_{ext} is the nanoantenna extinction cross section, σ_{abs} and σ_{sca} are the absorption and scattering cross sections respectively, $\sigma_{geo} = LD$ is the geometric cross section, A is the illuminated area, while N, L and D are the number, length and width of the illuminated nanoanten-

nas, respectively. The extinction efficiency essentially quantifies the capability of nanoantennas of collecting free-space radiation. **Figure 3b** depicts Q_{ext} as a function of frequency. The peak value is about 90 for all the samples, meaning that, under resonance condition, the effective cross section of our nanostructures increases by about 90 times. The experimentally extracted resonance properties of the nanoantenna arrays were also compared with the results of numerical simulations, performed using a finite integration technique-based commercial software (CST Microwave Studio). We considered gold nanoantennas with a rectangular section of 200 × 60 nm², capped with hemi-cylindrical terminations of radius equal to 100 nm. To better resemble the fabricated structures, all the nanoantenna edges were blended with a radius of curvature of 20 nm.

Furthermore, to simplify the simulated geometry while taking into account the influence of the silicon substrate, we considered nanoantennas entirely embedded in a homogenous medium of effective dielectric constant: $\varepsilon_{bg} = (1 + n_{Si}^2)/2$ [30], where $n_{Si} = 3.42$ is the refractive index of silicon in the THz region [31]. The gold dielectric constant was extracted from Ref. [32]. In all simulations, the nanoantennas were excited by a plane wave set at normal incidence, with polarization along the long axis of the nanostructures. In order to retrieve the nanoantenna resonance properties, we numerically evaluated the extinction efficiency Q_{ext} by extracting, from the simulations, the total absorption and scattering cross sections as a function of frequency. **Figure 4** illustrates the peak resonance wavelength λ_{res} as a function of the nanoantenna length (L = 30, 35, 40, 50 and 60 μm) for three cases: individual nanoantenna (numerical simulation, magenta squares), array of nanoantennas (numerical simulation, red squares) and experimental data (black crosses).

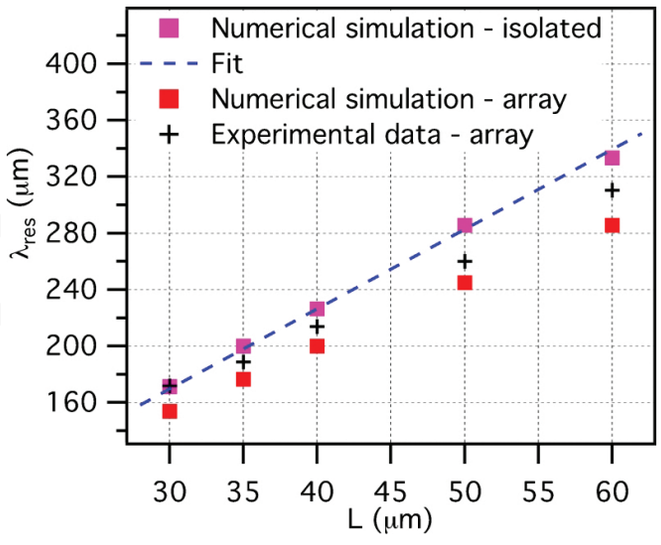

Figure 4. Resonance wavelength λ_{res} as a function of the nanoantenna length L. Numerical simulation for an isolated nanoantenna (magenta squares); best fit with the Fabry-Pérot model for an isolated THz antenna (dashed blue line); numerical simulations of the nanoantenna array (red squares); experimental data obtained from the resonance curves in **Figure 3** (black crosses). Adapted from with permission Ref. [22].

http://dx.doi.org/10.5772/66349

It is possible to observe that, as expected, the peak resonance wavelength increases linearly with the antenna length. This behavior can be further investigated using Eq. (2), and the simple Fabry-Pérot description discussed in the previous section (Section 2.1). Since δ is known to be of the order of the lateral dimension of the antenna [20, 26], it can be neglected in our case ($L \gg D$), and we can simply write: $\lambda_{res} = 2n_{eff}L$. The numerical results of the individual nanoantenna (magenta squares) can be therefore fitted with this equation to retrieve the effective refractive index. Notably, the obtained value, $n_{eff} = 2.83$, is higher than the background index employed in the simulations: $n_{bg} = \sqrt{\varepsilon_{bg}} = 2.52$. This means that a gold nanowire with lateral section as in the studied case (200 × 60 nm^2) cannot be considered as an ideal conductor at THz frequencies (i.e., the electric field of the propagating surface mode penetrates inside the metal). Comparing the numerical values obtained for the resonance of an individual nanoantenna (magenta squares) with the experimental data (black crosses in **Figure 4**), we notice that the experimental values slightly shift toward shorter wavelengths. This shift is attributed to the long-range dipolar interaction between neighboring nanoantennas in the array, which is known to affect the resonance properties of the system [16, 18]. Indeed, when the nanoantennas are organized in an array configuration, each element of the array is excited by a superposition of the incident electromagnetic field and the field scattered by the other elements. In order to corroborate this observation, we performed numerical simulations with periodic boundary conditions, to accurately evaluate the response of an array with a 20 μm spacing in both directions on the plane. These results are reported in **Figure 4** (red squares) and show a blue-shift of the array resonance frequency, confirming the origin of the shift observed in the experimental data. The residual difference between simulated and experimental values may be due to the uncertainty in the effective dielectric constants of the materials involved [33]. For applications exploiting the *local field enhancement* in close proximity of the nanoantennas, as it is the case with NETS, it is also important to investigate the *near-field resonance* properties of these nanostructures and compare them with the above reported *far-field resonance* characteristics. For the sake of simplicity, we considered here only the case of the array with L = 40 μm.

Figure 5a (magenta curve) shows the field enhancement factor F at the nanoantenna tip as a function of frequency, which is defined as the ratio of the local to the free-space field. A broad resonance centered at around 1.3 THz can be observed, with a peak field enhancement of a few hundreds. **Figure 5a** also displays the values of Q_{abs} and Q_{sca}, as well as their sum Q_{ext} (right axis). It is worth noticing that both absorption and scattering significantly contribute to the far-field resonance properties of the nanoantennas, featuring a peak at the same frequency of 1.5 THz. The near-field resonance peak thus results to be red-shifted (of about 200 GHz) with respect to the far-field peak. This behavior was previously observed in the optical frequency region and was attributed to plasmon damping [34–36]. In fact, by modeling the nanoantenna as a damped harmonic oscillator driven by the external electric field, the oscillator energy dissipation can be associated to the far-field extinction cross section of the nanoantenna, while the oscillator amplitude corresponds to the nanostructure near-field response. When damping is present, the peak of the oscillator amplitude is known to appear at a frequency that is lower than the natural frequency of the oscillator, while the maximum of the energy

dissipation remains un-shifted [34]. Therefore, the magnitude of the resonance shift between the near-field and far-field response is directly related to the total damping of the system, in terms of intrinsic ohmic loss in the metal and radiative damping [36]. In order to demonstrate the nature of this phenomenon at THz frequencies, we substituted gold and its realistic dielectric constant in the simulations with a perfect electric conductor (PEC, i.e., a material with infinite conductivity). **Figure 5b** shows the results of this procedure. As expected, in the case of a PEC, the contribution of absorption vanishes, and the far-field properties are ruled by scattering. In addition to a narrower resonance, the near-field peak was found to be almost coincident with the far-field peak. Thus, the red-shift of the near-field resonance observed in THz gold nanoantennas is mainly a consequence of ohmic damping. For an effective implementation of NETS, this effect has to be taken into account during the design of the nanostructures, in order to achieve the desired near-field response.

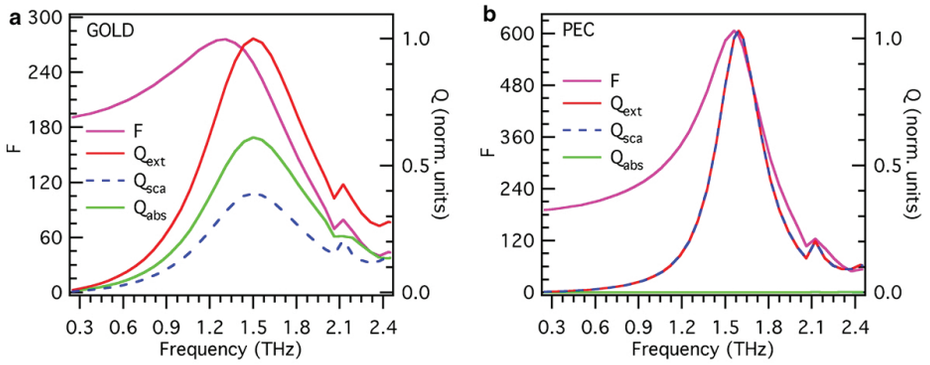

Figure 5. (a) Comparison between simulated near-field and far-field resonance spectra, for the array of gold nanoantennas with length L = 40 μm. Left vertical axis: field enhancement factor F (magenta line) as a function of frequency. Right vertical axis: normalized values of the extinction, scattering, and absorption efficiency Q_{ext}, Q_{sca} and Q_{abs} (red, dashed blue and green line, respectively) as a function of frequency. (b) Same as in (a), substituting gold with a perfect electric conductor (PEC). Reproduced with permission from Ref. [22].

3. Enhanced terahertz sensing and spectroscopy

As discussed in Section 2, metallic nanostructures can strongly increase the local THz electric field and can thus enhance the interaction of the incident radiation with a specimen placed in their proximity, this being the basic concept of NETS. Similar strategies, exploiting an augmented radiation-matter interaction, have been already successfully employed. For example, waveguide-assisted THz sensing [37] makes use of a guided geometry (e.g., in a parallel plate configuration), so that the effective interaction length can be increased up to several centimeters, enabling spectroscopic investigations of thin layers of biomolecules [38], explosives [39] and drugs [40]. The drawback of this approach is that the specimen has to be deposited throughout the whole length of the waveguide to effectively exploit the enhanced interaction. In a similar way, THz sensing using spoof plasmons (i.e., bound electromagnetic waves on corrugated metallic surfaces) also needs that the specimen under investigation is deposited

http://dx.doi.org/10.5772/66349

along the entire propagation length of the THz surface wave [41]. On the other hand, THz sensors based on metamaterials [2–4] have shown to be effective in sensing thin films of various compounds, down to the sub-micrometer level. Metamaterials indeed possess a narrowband resonance, whose position in frequency is strongly sensitive to the surrounding environment. For instance, Park et al. [2] recently proposed a metamaterial-based THz sensor capable of detecting live microorganism such as molds, yeast cells and bacteria. In particular, they prepared metallic arrays of square rings with a micro-gap at the center and functionalized the sensor with an antibody specific to bacteria (*E. coli*) in aqueous environment, in order to enable selective detection. The presence of the microorganisms at low densities was detected by probing (via THz-TDS [1]) the shift of the inductive-capacitive resonance, due to a change of the dielectric constant of the environment. As this and other examples can show, such type of THz metasurfaces is excellent refractive-index sensors, but they are not suitable for the identification of the spectroscopic signatures of the specimen under investigation.

In recently years, a new approach based on nanoslots [5–7] resonating at THz frequencies has been proposed by Park et al. [6], which has shown the possibility of strongly enhancing the THz absorption coefficient of molecules. In particular, they fabricated and tested a set of single nanoslot antennas (see illustration and SEM images in **Figure 6**) of fixed length (l = 90 μm) and varying widths (w = 50, 100, 200, 500, 1000 and 5000 nm) realized on a thin gold film of thickness h = 50 nm, for the smallest width w, and h = 100 nm for all the other cases, on a 500-μm-thick quartz substrate. The slots were prepared to have a resonance at around 0.87 THz, which matched the frequency peak of an absorption band of RDX (1,3,5-trinitroperhydro-1,3,5-trizine) molecules. **Figure 6c** shows the normalized resonant transmission (measured via far-field THz-TDS [1]) of these nanoslots as a function of the RDX amount that was drop-casted over the sample surface. Remarkably, a significant decrease of the resonant transmission intensity is already observed for an amount of 40 ng spread over a sample area of 8 mm^2, which corresponds to only 22 fg inside the slot cavity. This was made possible thanks to the high field enhancement achieved inside the slots at resonance that, in turn, increased the absorption coefficient of RDX molecules up to values higher than 100,000 cm^{-1}.

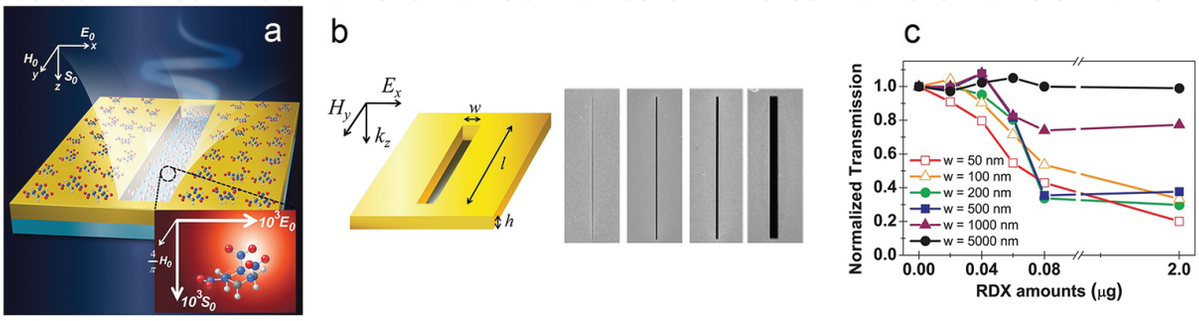

Figure 6. (a) Illustration of the RDX molecules spread over a THz nanoslot antenna. (b) Schematic of the nanoslot with definition of the relevant geometrical parameters, and SEM images of four samples: w = 50, 500, 1000 and 5000 nm. (c) Normalized resonant transmission measured at 0.87 THz for all the six samples, as function of the RDX amount. Adapted with permission from Ref. [6]. Copyright © 2013, American Chemical Society.

More recently, Lee et al. [7] demonstrated a nanoslot-array-based (see **Figure 7a**) THz sensing method which enables the selective detection of carbohydrate molecules (such as D-glucose, fructose, sucrose and cellulose). Here, two different nanoslot arrays with slot lengths l = 40 μm (f_{res} = 1.4 THz) and l = 35 μm (f_{res} = 1.7 THz) were designed, in order to match the absorption lines of D-glucose and fructose, respectively, following the sensing strategy reported in Ref. [6]. Even in this case, the strong field enhancement provided by the nanoslots (estimated to be about 50 for these slots featuring a width w = 500 nm) significantly increased the molecular absorption, enabling the detection of a specific sugar down to hundreds of micromoles. The selectivity of this system was verified by THz far-field imaging in transmission. In particular, the nanoslot array with its resonance matched to the absorption peak of fructose was used to discriminate this sugar from D-glucose. The upper-right corner of the array was covered with fructose and the lower-left corner with D-glucose (**Figure 7b**). **Figure 7c** shows the THz transmittance image of the sample under resonant conditions, highlighting the good selectivity of the sensor and its ability to discriminate the two types of sugars. The same system was also successfully employed to detect the sugars contained in popular sweetened beverages, including Coca-Cola, Pepsi-cola and Sprite. These works show the great potential of nanoslot-based sensors for the accurate detection of chemical compounds in the THz region. However, even in this case, no direct information regarding the main spectroscopic characteristics of the investigated sample (i.e., absorption peak position and bandwidth) was retrieved.

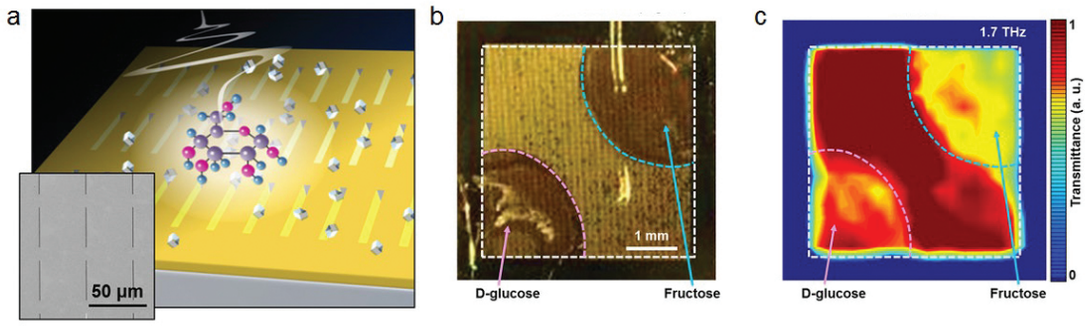

Figure 7. (a) Illustration and SEM detail of the nanoslot array-based THz sensing chip. (b) Photograph of the nanoslot array (l = 35 μm) after deposition of D-glucose and fructose (concentration: 250 mg/dL) in the two corners. (c) Normalized THz transmittance image of the array after deposition of the two sugar specimens. Adapted with permission from Ref. [7].

In the next section, we will discuss the use of engineered arrays of dipolar nanoantennas, reported in Section 2, to implement surface-enhanced spectroscopy in the THz spectral region. This technique basically translates the concept introduced by SEIRA for the infrared region into the THz domain and provides a valuable tool for THz spectroscopic investigations of ultra-low amounts of chemical compounds. In particular, we will summarize some of our recent results regarding the use of resonant dipole nanoantenna arrays to retrieve the spectroscopic response of a test sample: a monolayer of cadmium selenide quantum dots (CdSe QDs).

http://dx.doi.org/10.5772/66349

3.1. Resonant dipole nanoantenna arrays for enhanced THz spectroscopy

In Section 2, we discussed the properties of dipole nanoantenna arrays in the THz region. As mentioned, the simplest design for a resonant nanoantenna is represented by a metallic nanorod of length equal to about half of the effective wavelength of the exciting radiation (half-wavelength dipole nanoantenna) [20, 26]. In this configuration, the electric field concentrates into two sub-wavelength "hot-spots" at the antenna extremities. By moving from an isolated nanoantenna to nanostructures coupled end-to-end through a narrow gap, it is possible to increase and localize the electric field even further within such gap [18]. **Figure 8a** shows the nanoantenna arrangement employed in our investigation [23]. Several arrays of gold dipole nanoantennas (5 × 5 mm^2) were again fabricated on high-resistivity silicon substrates using e-beam lithography. We fixed the nanoantenna height and width at h = 60 nm and w = 200 nm, respectively. THz hot-spots featuring high field enhancement were obtained by coupling the nanoantennas along their long axis through nanogaps of nominal width of 20 nm (G_x in **Figure 8a**, see SEM image in **Figure 8b**). In order to demonstrate the capabilities of NETS, we selected CdSe QDs as test-bed nano-objects, since they are endowed with a clear phonon resonance in the THz range [42] (at 5.65 THz, as shown in **Figure 9b**). To tune the resonance of the nanoantenna arrays and match the QD phonon resonance, we performed extensive 3-D electromagnetic simulations, varying both the length L of the nanoantennas and their spacing G_y in the direction perpendicular to the antenna long axes (see **Figure 8a**). Indeed, as described in Section 2, its length [26] determines the resonance of a single nanoantenna and thus the main features of the spectral response of the whole array [22].

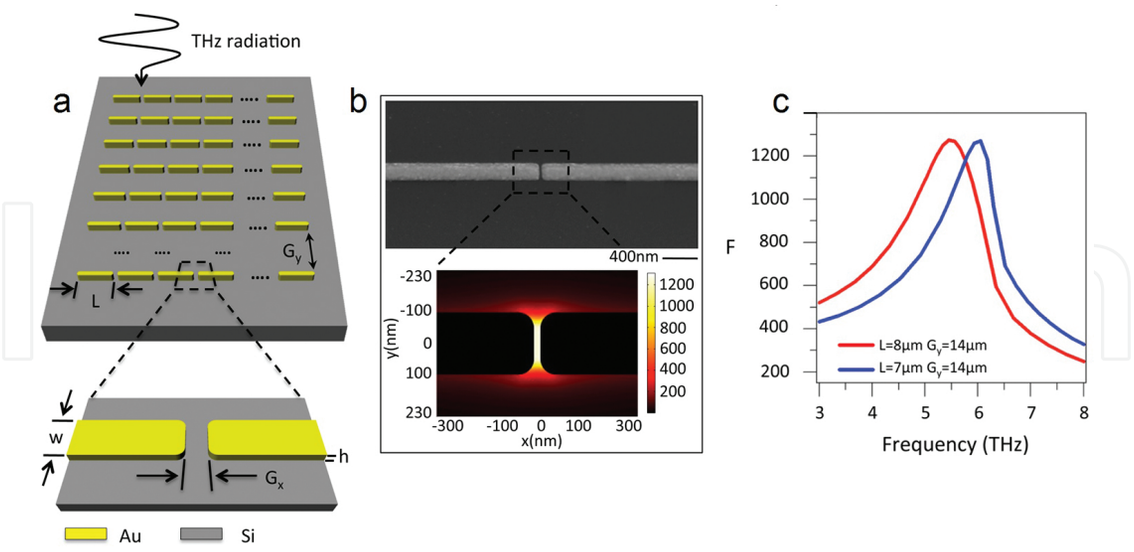

Figure 8. (a) Schematic illustration of the nanoantenna arrays used for the NETS demonstration. (b) SEM detail of a nanogap region (upper panel); 2D surface plot of the field enhancement factor F around the gap region at the QD resonance frequency, for L = 8 μm and G_y = 14 μm (lower panel). (c) F in the centre of the nanogap as a function of frequency, for two arrays with two different nanoantenna lengths L and same spacing G_y. Adapted with permission from Ref. [23]. Copyright © 2014, American Chemical Society.

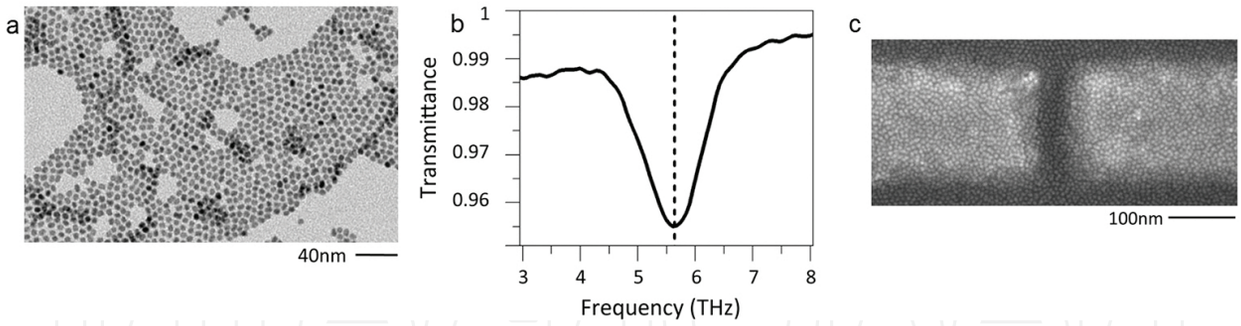

Figure 9. (a) TEM image of the synthesized CdSe QDs. (b) THz transmittance of a 100-nm-thick layer of CdSe QDs. (c) Magnification of a gap region covered with the dots, showing the uniformity of the QD layer. Adapted with permission from Ref. [23]. Copyright © 2014, American Chemical Society.

Additionally, the array spacing is also a critical parameter for engineering the frequency response of the nanostructures [22, 43]. Indeed, this spacing modifies the interaction between neighboring nanoantennas and has the ability to promote, by means of in-phase coupling, their collective excitation. This can result in resonance shift and narrowing, as well as lead to higher local fields. **Figure 8c** reports two examples of array geometries engineered to match the phonon resonance of the dots. In particular, it shows the field (amplitude) enhancement factor F in the center of the gap, being $F(x_0, y_0, z_0)$ defined here as the ratio of the local electric field at position (x_0, y_0, z_0) in the presence of the nanoantennas to the field in the same position considering a bare substrate with no structures. The effective localization of the THz electric field into sub-wavelength nano-volumes is illustrated in **Figure 8b** (lower part), which shows a 2D simulation of F around the gap region under resonant conditions. In the center of the nanogap, extremely high values of F (more than a thousand) are reached, which is fundamental for the successful realization of enhanced THz spectroscopy of nanomaterials. In fact, inside these gaps, the usually small effective absorption cross section of a nano-object at THz frequencies can be greatly amplified (up to more than a million times in the presented case), since it scales with $|F|^2$ [44].

3.1.1. Terahertz-enhanced spectroscopy of a monolayer of CdSe QDs

CdSe QDs were selected as a model system for our investigation since they can be prepared with high precision in shape and size, and they are known to form a compact and uniform layer, whose thickness can be accurately controlled. QDs with an average diameter of 5.2 nm were chemically synthesized using a previously developed protocol [45]. **Figure 9a** shows a transmission electron microscope (TEM) image of the dots, highlighting good size uniformity. The spectral response of the QDs was then retrieved through Fourier transform spectroscopy [46] (Bruker 70/v Fourier transform spectrometer) in a transmission configuration. **Figure 9b** presents the THz transmittance of a 100-nm-thick layer of QDs drop-casted on a bare silicon substrate. Their phonon resonance (Fröhlich mode) [42] is clearly visible as a transmission dip centered at ~5.65 THz. For the demonstration of NETS, a uniform monolayer of CdSe QDs was then spin-coated over the fabricated arrays (see detail of the gap region in **Figure 9c**).

http://dx.doi.org/10.5772/66349

Afterward, the THz transmittance of the four fabricated samples (with slightly shifted resonance frequencies) was again measured, and the results are shown in **Figure 10a**. For nonresonant excitation (not shown, polarization of the THz light set perpendicular to the long axis of the nanoantennas), the transmission of the samples was equivalent to the one of a bare silicon substrate, thus the presence of the QDs could not be detected. This result is in agreement with the QD response reported in **Figure 9b** for a 100-nm-thick layer. Indeed, for such thin layers, the transmittance change ΔT (i.e., the difference in transmittance between the reference silicon substrate and a substrate covered with the CdSe layer) results to be proportional to the layer thickness d ($\Delta T = 1 - e^{-\alpha d} \approx \alpha d$, where α is the layer attenuation coefficient). Considering that a transmission change of ~3.5% was measured for a 100-nm-thick layer (**Figure 9b**), a change of <0.2% should be expected for a monolayer, which is below the sensitivity of our experimental apparatus.

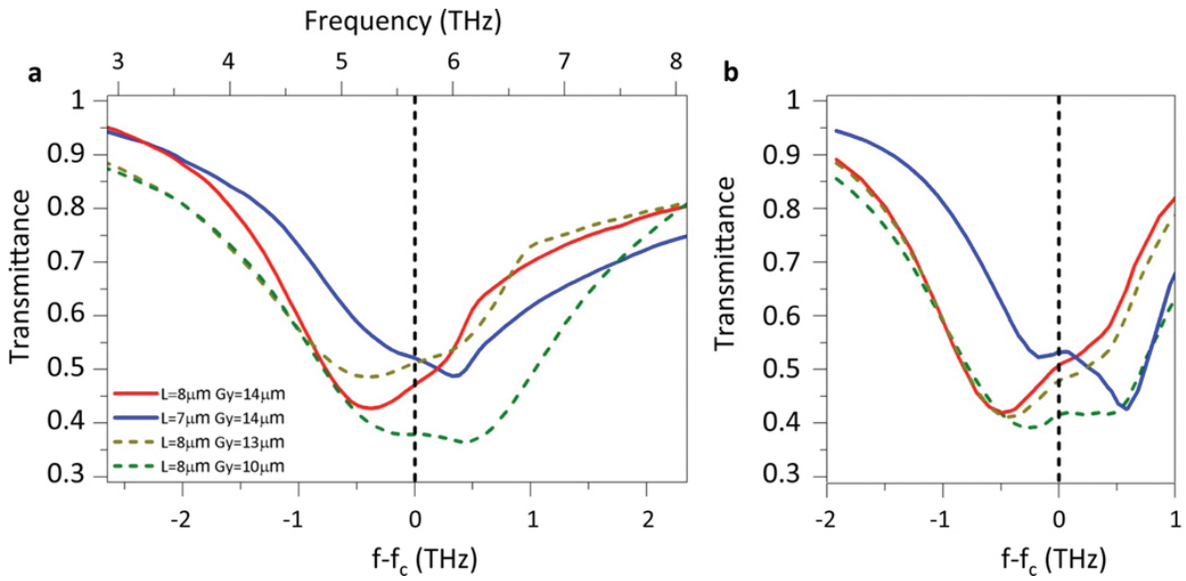

Figure 10. (a) Experimental transmittance of nanoantenna arrays covered with a monolayer of CdSe QDs, for different antenna lengths L and array spacings G_y (f_c is the central frequency of the phonon resonance). (b) Corresponding numerical simulations. Reproduced with permission from Ref. [23]. Copyright © 2014, American Chemical Society.

Conversely, when the nanoantennas were resonantly excited (polarization along their long axis), a clear anti-resonant peak, located in proximity of the QD phonon frequency f_c (black dotted line in **Figure 10**), was observed over the resonance response of the arrays (**Figure 10a**). This Fano-like behavior [47] arises from the interference between the nanoantenna mode and the QD phonon resonance. The result is similar to the one traditionally observed in SEIRA measurements [48–50]. It is worth underlining that the Fano-like anti-resonant feature is clearly visible for all the tested arrays, which possess distinct nanoantenna resonance frequencies. This demonstrates that only a coarse alignment between the phonon mode of the QDs and the nanoantenna resonance is necessary to observe the effect. Furthermore, the interference peak always appears in the spectrum in correspondence of the QD vibrational frequency (black dashed line), as expected for a Fano-like interference. The observed coupling

between the nanoantenna resonant mode and the QD phonon line was also investigated through extensive numerical simulations. In order to reduce the required meshing elements and thus the computational time, we considered a uniform layer with thickness equal to the QD diameter (5.2 nm) and permittivity as in Ref. [51], which reports the THz response of CdSe QDs with a diameter (6.3 nm) similar to the ones investigated in our work. The results of the simulations are reported in **Figure 10b**. As can be seen, they well reproduce the overall behavior of the system and are in good agreement with the experimental measurements.

3.1.2. Absorption enhancement

The results presented in **Figure 10** show that NETS allows sensing ultra-low quantity of compounds (in our proof-of-concept experiment, a monolayer of CdSe QDs) through the formation of a Fano-like resonance. This is clearly visible and corresponds to a spectral feature of the specimen under investigation, which couples with the nanoantenna mode of the array. As already discussed in the beginning of this section, NETS relies on the fact that a specimen absorption is strongly sensitive to the local electric field, which can be greatly increased (see field enhancement values in **Figure 8c**) in proximity of nanoantennas. In this regard, we made use of numerical simulations to quantitatively estimate this effect in the case of our NETS arrays. The overall array absorption enhancement η_{tot} at the QD phonon resonance frequency ν_{ph} can be evaluated by calculating the surface integral of $|F|^2$ at resonance, and dividing it by the total sensing area A = 25 mm^2:

$$\eta_{tot}\left(\upsilon_{ph}\right) = \frac{\iint_{tot}\left|F(\upsilon_{ph},x,y)\right|^2 dxdy}{A} \tag{6}$$

In particular, for the case of the array with L = 8 μm and G_y = 14 μm, whose characterization is reported in **Figure 10a** (red line), we find $\eta_{tot} \approx 70$, which is a significant result considering that the nanoantenna covering factor is only 1.4%. In a similar way, we can also estimate the contribution of the QDs situated in the nanogap regions to the overall absorption. To this end, we can compare the surface integral of $|F|^2$ calculated over the area covered by the nanogaps with the one calculated over the entire array:

$$\frac{\eta_{gap}\left(\upsilon_{ph}\right)}{\eta_{tot}\left(\upsilon_{ph}\right)} = \frac{\iint_{gap}\left|F(\upsilon_{ph},x,y)\right|^2 dxdy}{\iint_{tot}\left|F(\upsilon_{ph},x,y)\right|^2 dxdy} \tag{7}$$

Considering again the array with L = 8 μm and G_y = 14 μm, we find η_{gap}/η_{tot} = 0.52. This means that about half of the total absorption of the monolayer occurs in the nanogap regions. This result is of great relevance since the nanogaps cover an area ~30,000 times smaller than the

total sensing surface, and each of them contains roughly 130 QDs (visual estimate from the SEM image in **Figure 9c**).

3.1.3. Analytical description through a two coupled harmonic oscillator model

A direct and simple analytical model can be used to describe the NETS measurements, in order to shed more light on the underlying physical mechanism and extract the main spectroscopic information of the investigated specimen. Indeed, the observed Fano-like interference can be modeled by considering a system composed of two coupled harmonic oscillators [52, 53]: one representing the nanoantenna resonance mode and the other the phonon mode of the QDs. The first oscillator is characterized by a resonance frequency $\omega_{pl} = 2\pi\nu_{pl}$ and damping $\gamma_{pl} = 2\pi\Delta\nu_{pl}$ ($\Delta\nu_{pl}$ being the full width at half maximum of the resonance), while the second one has a resonance frequency $\omega_{ph} = 2\pi\nu_{ph}$ and a damping factor $\gamma_{ph} = 2\pi\Delta\nu_{ph}$. The two systems can be connected together through the coupling constant g. Since the phonon mode of the QD monolayer is weakly excited by the far-field radiation, we consider the first (nanoantenna) oscillator to be the one excited by the external driving force: $fe^{i\omega t}$. Under this approximation, the equations of motion can be written as:

$$\begin{aligned} \ddot{x}_{pl} + \gamma_{pl}\dot{x}_{pl} + \omega_{pl}^2 x_{pl} + g x_{ph} &= f e^{i\omega t} \\ \ddot{x}_{ph} + \gamma_{ph}\dot{x}_{ph} + \omega_{ph}^2 x_{ph} + g x_{pl} &= 0 \end{aligned} \tag{8}$$

Assuming a harmonic displacement, $x_{pl,ph} = c_{pl,ph}e^{i\omega t}$, the amplitude of the nanoantenna oscillator can be written as:

$$c_{pl} = \frac{\omega_{ph}^2 + i\gamma_{ph}\omega - \omega^2}{\left(\omega_{pl}^2 + i\gamma_{pl}\omega - \omega^2\right)\left(\omega_{ph}^2 + i\gamma_{ph}\omega - \omega^2\right) - g^2} f \tag{9}$$

Figure 11 shows how the absolute value squared of the nanoantenna oscillator amplitude $\left|c_{pl}\right|^2$ (blue solid line) can properly reproduce the main characteristics of our experimental results (red circles, representing the normalized extinction efficiency, extracted from the experimental transmittance, for the array with L = 8 μm and G_y = 10 μm). In particular, the model well reconstructs the anti-resonant Fano-like feature in correspondence of the QD phonon resonance. A direct comparison between this model and NETS experimental results can be used to extract the main spectroscopic properties of the specimen under investigation, in terms of absorption peak position and bandwidth. In the studied case, by fitting the experimental data, we obtained values for the QDs phonon resonance frequency ($\nu_{ph,\,\mathrm{model}} = 5.72$ THz) and

bandwidth ($\Delta\nu_{ph,\,\mathrm{model}} = 1.12$ THz) that were in good agreement with the experimental ones ($\nu_{ph,\,exp} = 5.64$ THz and $\Delta\nu_{ph,\,\mathrm{exp}} = 1.15$ THz, retrieved from the measurement shown in **Figure 9b**).

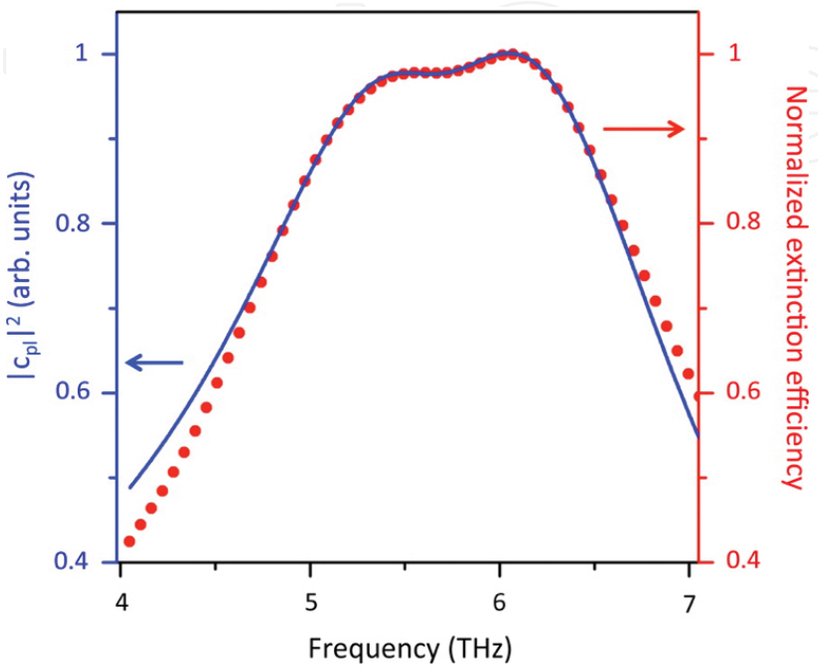

Figure 11. $\left|c_{pl}\right|^2$ as a function of frequency (blue) and normalized extinction efficiency σ_{ext} (from the experimental transmittance T as $\sigma_{ext} \propto 1 - T$ of the array (L = 8 μm and G_y = 10 μm) covered with QDs (red circles). Reproduced with permission from Ref. [23]. Copyright © 2014, American Chemical Society.

4. Conclusion

In this chapter, we have shown how to design arrays of THz nanoantennas to perform enhanced THz spectroscopy. In the beginning, we have discussed the properties of metals at THz frequencies, retrieving the complex dielectric function through the Drude model. In order to describe the resonance response of an individual dipole nanoantenna, the basic element of our investigation, we have introduced a Fabry-Pérot resonator model for a surface wave over a metallic wire. Through this simple quasi-analytical model, the resonance characteristics of a nanoantenna can be quickly evaluated, avoiding time-consuming numerical simulations. Afterward, we have presented both numerical and experimental results regarding the electromagnetic response of THz nanoantenna arrays. In particular, we have shown that, by varying the length of the nanoantennas, the resonance peak of the array can be tuned to cover the THz band offered by standard THz sources. In addition, we have discussed the resonance shift that arises between the near- and far-field responses of nanoantennas. We have shown

that, in these devices, the near-field resonance peak can substantially red-shift in comparison to the far-field peak, due to the ohmic damping within the metal. This is an important information for the practical implementation of NETS, since the targeted absorption enhancement relies on the local field in proximity of the nanostructures. Subsequently, we have summarized some recent results reported in the literature on THz sensing via metamaterials and metallic nanostructures. Finally, we have presented the demonstration of NETS, reporting results obtained on a monolayer of CdSe QDs by means of engineered nanoantenna arrays coupled through nanogaps. As a result of the direct coupling between the nanoantenna mode and the phonon resonance of the QDs, the formation of an evident Fano-like interference (centered at the phonon resonance frequency) over the array response was observed. The high field enhancement (more than one thousand) obtained in the center of the nanogaps enabled an increase of the absorption cross section of the QDs up to more than a million times, which in turn allowed the ultrasensitive characterization of the QD spectroscopic signature. Moreover, we have shown that a simple model based on coupled harmonic oscillators can be employed to reproduce the Fano-like interference and extract the main spectroscopic characteristics (absorption peak frequency and bandwidth) of the investigated specimen. NETS has thus been proven to be a useful tool for the spectroscopic characterization of ultra-low quantities of nanomaterials. Very recently, using a similar strategy, Ueno et al. [54] performed surface-enhanced THz spectroscopy of amino acid molecules by means of arrays of gold dipole nanoantennas. This promising result shows that NETS can also be effectively extended to ensembles of molecules, and specifically to organic compounds of biological relevance.

Author details

Riccardo Piccoli[1*], Andrea Rovere[1], Andrea Toma[2], Roberto Morandotti[1] and Luca Razzari[1*]

*Address all correspondence to: riccardo.piccoli@emt.inrs.ca and luca.razzari@emt.inrs.ca

1 INRS-EMT, Varennes, Québec, Canada

2 Istituto Italiano di Tecnologia (IIT), Genova, Italy

References

[1] S.L. Dexheimer. Terahertz spectroscopy: principles and applications. Boca Raton, Florida, US: CRC Press; 2008.

[2] S. J. Park, J. T. Hong, S. J. Choi, H. S. Kim, W. K. Park, S. T. Han, J. Y. Park, S. Lee, D. S. Kim, Y. H. Ahn. Detection of microorganisms using terahertz metamaterials, Sci. Rep. 2014;4(4988).

[3] J. F. O'Hara, R. Singh, I. Brener, E. Smirnova, J. Han, A. J. Taylor, W. Zhang. Thin-film sensing with planar terahertz metamaterials: sensitivity and limitations. Opt. Express, 2008;16(3):1786–1795.

[4] F. D'Apuzzo, P. Candeloro, F. Domenici, M. Autore, P. Di Pietro, A. Perucchi, P. Roy, S. Sennato, F. Bordi, E. M. Di Fabrizio, S. Lupi. Resonating terahertz response of periodic arrays of subwavelength apertures. Plasmonics 2014;10(1):45–50.

[5] M. A. Seo, H. R. Park, S. M. Koo, D. J. Park, J. H. Kang, O. K. Suwal, S. S. Choi, P. C. M. Planken, G. S. Park, N. K. Park, Q. H. Park, D. S. Kim. Terahertz field enhancement by a metallic nano slit operating beyond the skin-depth limit. Nat. Photonics. 2009;3:152–156.

[6] H. R. Park, K. J. Ahn, S. Han, Y. M. Bahk, N. Park, D. S. Kim. Colossal absorption of molecules inside single terahertz nanoantennas. Nano Lett. 2013;13(4):1782–1786.

[7] D. K. Lee, J. H. Kang, J. S. Lee, H. S. Kim, C. Kim, J. H. Kim, T. Lee, J. H. Son, Q. H. Park M. Seo. Highly sensitive and selective sugar detection by terahertz nano-antennas. Sci. Rep. 2015;5:154–159.

[8] R. Aroca, editor. Surface-enhanced vibrational spectroscopy. Chichester, UK: John Wiley & Sons; 2006.

[9] M. Fleischmann, P. J. Hendra, A. J. McQuillan. Raman spectra of pyridine adsorbed at a silver electrode. Chem. Phys. Lett. 1974;26(2):163–166.

[10] K. Kneipp, M. Moskovits, H. Kneipp. Surface-enhanced Raman scattering: physics and applications. Berlin, Germany: Springer-Verlag; 2006.

[11] S. Nie, S. R. Emory. Probing single molecules and single nanoparticles by surface-enhanced Raman scattering. Science. 1997;275:1102–1106.

[12] K. Kneipp, Y. Wang, H. Kneipp, L. T. Perelman, I. Itzkan, R. R. Dasari, M. S. Feld. Single molecule detection using surface-enhanced Raman scattering (SERS). Phys. Rev. Lett. 1997;78:1667–1670.

[13] M. Chirumamilla, A. Toma, A. Gopalakrishnan, G. Das, R. Proietti Zaccaria, R. Krahne, E. Rondanina, M. Leoncini, C. Liberale, F. De Angelis, E. Di Fabrizio. 3D nanostar dimers with a sub-10-nm gap for single-/few-molecule surface-enhanced Raman scattering. Adv. Mater. 2014;26:2353–2358.

[14] A. Hartstein, J. R. Kirtley, J. C. Tsang. Enhancement of the infrared absorption from molecular monolayers with thin metal overlayers. Phys. Rev. Lett. 1980;45:201–204.

[15] M. Osawa, K.-I Ataka, K. Yoshii, Y. Nishikawa. Surface-enhanced infrared spectroscopy: the origin of the absorption enhancement and band selection rule in the infrared spectra of molecules adsorbed on fine metal particles. Appl. Spectrosc. 1993;47:1497–1502.

[16] R. Adato, A. A. Yanika, J. J. Amsdenc, D. L. Kaplanc, F. G. Omenetto, M. K. Honge, S. Erramillib, H. Altug. Ultra-sensitive vibrational spectroscopy of protein monolayers with plasmonic nanoantenna arrays. Proc. Natl. Acad. Sci. 2009;106:19227–19232.

[17] L. Novotny, B. Hecht. Principle of nano-optics. 2nd ed. Cambridge: University Press; Cambridge, UK 2012.

[18] P. Biagioni, J.-S. Huang, B. Hecht. Nanoantennas for visible and infrared radiation. Rep. Prog. Phys. 2012;75 (024402).

[19] M. Dressel, G. Grüner. Electrodynamics of solids: optical properties of electrons in matter. 1st ed. Cambridge: Cambridge University Press; 2002.

[20] E. Cubukcu, F. Capasso. Optical nanorod antennas as dispersive one-dimensional Fabry-Pérot resonators for surface plasmons. Appl. Phys. Lett. 2009;95 (201101).

[21] L. Razzari, A. Toma, M. Shalaby, M. Clerici, R. Proietti Zaccaria, C. Liberale, S. Marras, I. A. I. Al-Naib, G. Das, F. De Angelis, M. Peccianti, A. Falqui, T. Ozaki, R. Morandotti, E. Di Fabrizio. Extremely large extinction efficiency and field enhancement in terahertz resonant dipole nanoantennas. Opt. Express. 2011;19:26088–26094.

[22] L. Razzari, A. Toma, M. Clerici, M. Shalaby, G. Das, C. Liberale, M. Chirumamilla, R. Proietti Zaccaria, F. De Angelis, M. Peccianti, R. Morandotti, E. Di Fabrizio. Terahertz dipole nanoantenna arrays: resonance characteristics. Plasmonics. 2013;8(1):133–138.

[23] A. Toma, S. Tuccio, M. Prato, F. De Donato, A. Perucchi, P. Di Pietro, S. Marras, C. Liberale, R. Proietti Zaccaria, F. De Angelis, L. Manna, S. Lupi, E. Di Fabrizio, L. Razzari. Squeezing terahertz light into nanovolumes: nanoantenna enhanced terahertz spectroscopy (NETS) of semiconductor quantum dots. Nano Lett. 2015;15(1):386–391.

[24] M. G. Blaber, M. D. Arnold, M. J. Ford. Search for the ideal plasmonic nanoshell: the effects of surface scattering and alternatives to gold and silver. J. Phys. Chem. C. 1998;113(8):3041–3045.

[25] L. Novotny, C. Hafner. Light propagation in a cylindrical waveguide with a complex, metallic, dielectric function. Phys. Rev. E. 1994;50: 4094–4106.

[26] L. Novotny. Effective wavelength scaling for optical antennas, Phys. Rev. Lett. 2007;98(266802).

[27] R. Gordon. Reflection of cylindrical surface waves. Opt. Express. 2009;17(21):18621–18629.

[28] R. Gordon. Vectorial method for calculating the Fresnel reflection of surface plasmon polaritons Phys. Rev. B. 2006;74(153417).

[29] Q. Wu, X-C. Zhang. Free-space electro-optic sampling of terahertz beams. Appl. Phys. Lett. 1995;67:3523–3525.

[30] F. Neubrech, T. Kolb, R. Lovrincic, G. Fahsold, A. Pucci, J. Aizpurua, T. W. Cornelius, M. E. Toimil-Molares, R. Neumann and S. Karim. Resonances of individual metal nanowires in the infrared. Appl. Phys. Lett. 2006;89(253104).

[31] E. D. Palik. Handbook of optical constants of solids. San Diego: Academic; 1998.

[32] M. Walther, D. G. Cooke, C. Sherstan, M. Hajar, M. R. Freeman, F. A. Hegmann. Terahertz conductivity of thin gold films at the metal-insulator percolation transition. Phys. Rev. B. 2007;76(125408).

[33] K-P. Chen, V. P. Drachev, J. D. Borneman, A. V. Kildishev, V. M. Shalaev. Drude relaxation rate in grained gold nanoantennas. Nano Lett. 2010;10:916–922.

[34] J. Chen, P. Albella, Z. Pirzadeh, P. Alonso-González, F. Huth, S. Bonetti, V. Bonanni, J. Åkerman, J. Nogués, P. Vavassori, A. Dmitriev, J. Aizpurua, R. Hillenbrand. Plasmonic nickel nanoantennas. Small. 2011;7:2341–2347.

[35] B. M. Ross, L. P. Lee. Comparison of near- and far-field measures for plasmon resonance of metallic nanoparticles. Opt. Lett. 2009;34:896–898.

[36] J. Zuloaga, P. Nordlander. On the energy shift between near-field and far-field peak intensities in localized plasmon systems. Nano Lett. 2011;11:1280–1283.

[37] G. Gallot, S. P. Jamison, R. W. McGowan, D. J. Grischkowsky. Terahertz waveguides. Opt. Soc. Am. B. 2000;17:851–863.

[38] N. Laman, S. S. Harsha, D. Grischkowsky, J. S. Melinger. High-resolution waveguide THz spectroscopy of biological molecules. Biophys. J. 2008;94:1010–1020.

[39] J. S. Melinger, N. Laman, D. Grischkowsky. The underlying terahertz vibrational spectrum of explosives solids. Appl. Phys. Lett. 2008;93(011102)

[40] N. Laman; S. S. Harsha, D. Grischkowsky. Narrow-line waveguide terahertz time-domain spectroscopy of aspirin and aspirin precursors. Appl. Spectrosc. 2008;62:319–326.

[41] B. Ng, S. M. Hanham, J. Wu, A. I. Fernández-Domínguez, N. Klein, Y. Fook Liew M. B. H. Breese, M. Hong, S. A. Maier. Broadband terahertz sensing on spoof plasmon surfaces. ACS Photonics. 2014;1:1059–1067.

[42] M. I. Vasilevskiy, A. G. Rolo, M. V. Artemyev, S. A. Filonovich, M. J. M. Gomes, Yu. P. Rakovich. FIR absorption in CdSe quantum dot ensembles. Phys. Status Sol. B. 2001;224:599–604.

[43] W. Zhou, T. W. Odom. Tunable subradiant lattice plasmons by out-of-plane dipolar interactions. Nat. Nanotechnol. 2011;6:423–427.

[44] L. Novotny, N. van Hulst. Antennas for light. Nat. Photonics. 2011;5:83–90.

[45] L. Carbone, C. Nobile, M. De Giorgi, F. Della Sala, G. Morello, P. Pompa, M. Hytch, E. Snoeck,A. Fiore, I. R. Franchini, M. Nadasan, A. F. Silvestre, L. Chiodo, S. Kudera, R.

Cingolani, R. Krahne, L. Manna. Synthesis and micrometer-scale assembly of colloidal CdSe/CdS nanorods prepared by a seeded growth approach. Nano Lett. 2007;7:2942–2950.

[46] P. R. Griffiths, J. A. de Haseth. Fourier transform infrared spectrometry. Hoboken, NJ: John Wiley & Sons; 2007.

[47] U. Fano. Effects of configuration interaction on intensities and phase shifts. Phys. Rev. 1961;124:1866–1878.

[48] C. Huck, F. Neubrech, J. Vogt, A. Toma, D. Gerbert, J. Katzmann, T. Härtling, A. Pucci. Surface-enhanced infrared spectroscopy using nanometer-sized gaps. ACS Nano. 2014;8:4908–4914.

[49] F. Neubrech A. Pucci, T. W. Cornelius, S. Karim, A. García-Etxarri, J. Aizpurua. Resonant Plasmonic and Vibrational Coupling in a Tailored Nanoantenna for Infrared Detection. Phys. Rev. Lett. 2008;101(157403).

[50] C. D'Andrea, J. Bochterle, A. Toma, C. Huck, F. Neubrech, E. Messina, B. Fazio, O. M. Maragò, E. Di Fabrizio, M. Lamy de La Chapelle, P. G. Gucciardi, A. Pucci. Optical nanoantennas for multiband surface-enhanced infrared and Raman spectroscopy. ACS Nano. 2013;7:3522–3531.

[51] P. K. Mandal, V. Chikan. Plasmon−phonon coupling in charged n-Type CdSe quantum dots: a THz time-domain spectroscopic study. Nano Lett. 2007;7:2521–2528.

[52] Y. S. Joe, A. M. Satanin, C. S. Kim. Classical analogy of Fano resonances. Phys. Scr. 2006;74:259–266.

[53] B. Gallinet, O. J. F. Martin. Ab initio theory of Fano resonances in plasmonic nanostructures and metamaterials. Phys. Rev. B. 2011;83(235427).

[54] K. Ueno, S. Nozawa, H. Misawa. Surface-enhanced terahertz spectroscopy using gold rod structures resonant with terahertz waves. Opt. Express. 2015;23:28584–28592.

IntechOpen